MATERIALS SCIENCE

A path for lignin valorization via additive manufacturing of high-performance sustainable composites with enhanced 3D printability

Ngoc A. Nguyen[1]*†, Sietske H. Barnes[1], Christopher C. Bowland[1†], Kelly M. Meek[1], Kenneth C. Littrell[2], Jong K. Keum[2,3], Amit K. Naskar[1]*†

We report the manufacture of printable, sustainable polymer systems to address global challenges associated with high-volume utilization of lignin, an industrial waste from biomass feedstock. By analyzing a common three-dimensional printing process—fused-deposition modeling—and correlating the printing-process features to properties of materials such as acrylonitrile-butadiene-styrene (ABS) and nylon, we devised a first-of-its-kind, high-performance class of printable renewable composites containing 40 to 60 weight % (wt %) lignin. An ABS analog made by integrating lignin into nitrile-butadiene rubber needs the presence of a styrenic polymer to avoid filament buckling during printing. However, lignin-modified nylon composites containing 40 to 60 wt % sinapyl alcohol–rich, melt-stable lignin exhibit enhanced stiffness and tensile strength at room temperature, while—unexpectedly—demonstrating a reduced viscosity in the melt. Further, incorporation of 4 to 16 wt % discontinuous carbon fibers enhances mechanical stiffness and printing speed, as the thermal conductivity of the carbon fibers facilitates heat transfer and thinning of the melt. We found that the presence of lignin and carbon fibers retards nylon crystallization, leading to low-melting imperfect crystals that allow good printability at lower temperatures without lignin degradation.

INTRODUCTION

On-demand free-form fabrication of soft materials having complex shapes with precise dimensions and desired performance in specific environments, either as a component of a machine or as any object including biological implants, is an emerging challenge (*1*–*6*). These soft materials are mostly polymeric in nature. Numerous relevant manufacturing technologies, collectively called additive manufacturing, are being explored for these polymeric products (*7*–*10*). Among all the methods, fused deposition modeling (FDM) or melt-extrusion three-dimensional (3D) printing is the most popular, and with FDM, 3D objects are produced through sequential deposition of molten polymer layers. For FDM, deposition of polymer melt is achieved by pushing a solid monofilament of polymer (diameter, 2 to 3 mm) through a cylindrical heated chamber where it melts. The molten mass is then pushed through a hot nozzle of a precise dimension by the solid filament that acts as a piston. The nozzle head usually traverses in the *x*–*y* plane for controlled deposition of the molten layer that gradually solidifies on a platform, which progresses in the *z* direction to accommodate deposition of the next layer (*3*, *5*–*7*). For FDM, however, not all melt-extrudable polymers exhibit efficient printability.

Contrasting printability of melt-processed polymers arises primarily due to the differences in their rheological characteristics both in the molten state and in their solid form. Further, the addition of functional fillers and additives in the polymer matrix changes the materials' characteristics and their printability. For example, particulate-filled polymers with higher melt viscosity often cause clogging at the printing nozzle and reduce deposition throughput. When a solid polymer filament is used as a piston and fed through the heated printer head assembly, there is a limiting rate of filament loading beyond which shear failure of the filament occurs between the pinch roller and the drive wheels (*11*). In addition, the filament must exhibit a minimal stiffness to avoid buckling before entering the heated zone. Resistance to flow inside the heated chamber may occur if the heat transfer from the wall of the chamber to the bulk of the filament remains poor. Obviously, shear-thinning of the polymer melt at higher shear rate offers better flow through the nozzle; however, higher zero-shear viscosity of the material and rapid solidification via improved heat dissipation are highly desired to eliminate the dimensional instability of the printed layer. Thus, the shear rate and temperature-dependent rheological parameters and the thermal conductivity of a polymer play key roles in deciding the fate of a polymer filament through an FDM device (*11*, *12*). For a specific polymer, shear-thinning behavior can also be exploited to lower viscosity by manipulating the polymer throughput rate and the nozzle diameter of the printer head.

Using heat to reduce viscosity is not an option if the polymer filament has poor thermal stability. FDM with such materials remains a grand challenge. With this in mind, we wish to develop printable polymeric materials primarily consisting of a plant biomass derivative, namely, lignin (Fig. 1). Lignin is the second most abundant renewable material after cellulose. It forms the supporting skeleton surrounding cellulose microfibrils (*13*). While cellulose from deconstructed biomass is a feedstock for paper, chemicals, fuels, and plastics manufacturing, the lignin fraction remains underutilized (*14*–*16*). Whole lignocellulosic materials (not deconstructed) usually do not melt; lignin degrades at high temperature and forms a rigid char, resulting in increased resistance to flow or deformation. Some isolated lignin fractions, particularly those with linear sinapyl alcohol units from hardwood (HW) plants (*17*, *18*) and oligomeric fraction of extracted softwood (SW) lignins (*19*–*21*), however, exhibit good melt stability. In this article, we discuss the molecular and rheological characteristics of two different

[1]Materials Science and Technology Division, Oak Ridge National Laboratory, Oak Ridge, TN 37831, USA. [2]Neutron Scattering Division, Oak Ridge National Laboratory, Oak Ridge, TN 37831, USA. [3]Center for Nanophase Materials Sciences, Oak Ridge National Laboratory, Oak Ridge, TN 37831, USA.
*Corresponding author. Email: nguyenna@ornl.gov (N.A.N); naskarak@ornl.gov (A.K.N.)
†Present address: Chemical Sciences Division, Oak Ridge National Laboratory, Oak Ridge, TN 37831, USA.

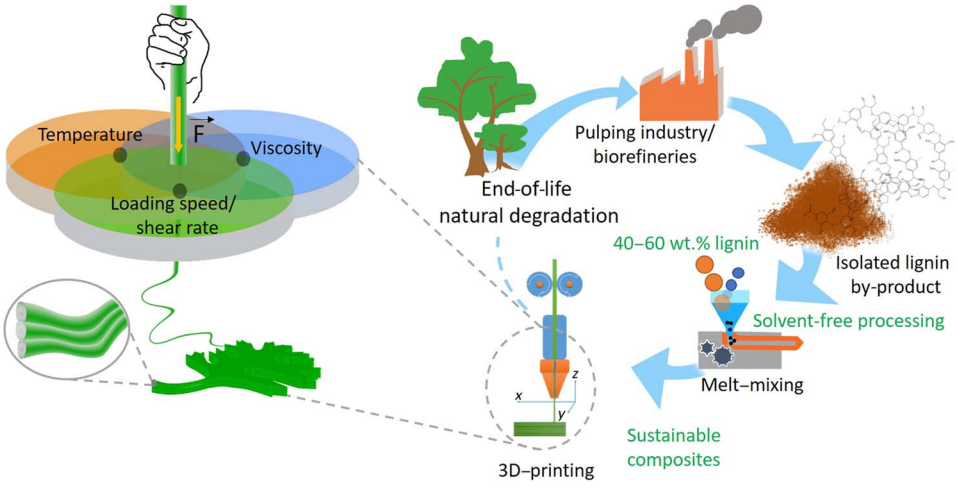

Fig. 1. Printability of renewable composites. Sustainable 3D-printed products made from 40 to 60 wt % lignin containing polymeric materials formulated by a solvent-free process and exhibiting appropriate processability constrained by an optimum window of temperature, shear rate and/or filament feeding rate, and viscosity.

lignins that are either coniferyl alcohol or sinapyl alcohol dominant and correlate the effects of these structural units on specific interactions in their nearly equal mass alloy with different polymeric host matrices.

We apply melt rheology to determine compositions for lignin-based renewable, fiber-reinforced composites that demonstrate extraordinary mechanical properties and superior 3D printability by FDM. To the best of our knowledge, this is the first report of a renewable polymer that contains ~50 weight % (wt %) unmodified lignin and outperforms commodity thermoplastics, such as high-impact polystyrene (HIPS) resins, in terms of both mechanical performance and 3D printability. We demonstrate that our material exhibits reduced viscosity and facile printability even after loading 16 wt % chopped carbon fibers (CFs) as a reinforcing agent. Although the incorporation of discontinuous CF in the resin matrices increases viscosity, we find that these compositions exhibit viscosities lower than that of a common neat, petroleum-derived printable resin.

The market for materials used in melt extrusion–based printing is very large, and it is currently dominated by petroleum-based thermoplastics. Despite the benefits that wood and plant-based materials offer for additive manufacturing, the market remains limited with the notable exception of polylactic acid (PLA) for FDM. However, PLA has poor thermal and mechanical properties, which render it unacceptable for most engineering applications. While efforts to improve the thermomechanical properties of PLA are promising (*22*), other researchers have opted to study alternative biofeedstocks (*23*). The results we describe here open a new avenue of using isolated lignin as a feedstock for formulating 3D-printing materials that have superior mechanical and printing characteristics. Our findings should result in additional revenue streams for biomass-processing industries via lignin valorization. This report will also be of considerable interest to researchers working with renewable materials, additive manufacturing, and sustainability.

RESULTS AND DISCUSSION

Chemical structure and melt processability of lignin

In this study, the structure and properties of the selected lignins are investigated and correlated to their processability for FDM. The molecular architectures of coniferyl alcohol–rich SW and sinapyl alcohol–rich HW lignins strongly influence their thermal and rheological properties. The very low molar mass (only a few thousand daltons) of these neat phenolic oligomers allows for melt and solution processing but causes brittleness. Lignin alone cannot form a freestanding film. Therefore, the direct usage of lignin as a polymeric material remains limited. Plasticizers and additives have been commonly used to modify the materials. We reported earlier that combining lignin with the nitrile group containing rubbers produced a new class of melt-processable thermoplastic elastomers. These exhibited unique yield stress and high toughness primarily due to morphology control of the dispersed lignin phase (*17*, *19*). However, the relationship between lignin's molecular structure and material processability has not been properly discerned. In this study, the lignin structural units are correlated to the rheological properties to prepare renewable 3D-printable materials that exhibit outstanding printability and mechanical performance. A processing window, which offers a quantitative measure of the material's printability, was determined on the basis of viscosity change with temperature and shear rate. This illustrates that lignin type plays a role in printability.

The measured rheological data of the lignin samples and their representative molecular architectures are presented in Fig. 2. The detailed structure and functional group analyses of the lignins were discussed in our recent report (*20*). The dominance of β-O-4′ linkage in organosolv HW lignin (highlighted in orange and marked as structural unit A, see Fig. 2A) containing long aliphatic Cα-Cβ-Cγ-OH chains offers flexibility in the lignin segments. In addition, the ^{13}C-NMR (nuclear magnetic resonance) data in Fig. 2C indicate dominance of a chemical shift from 10 to 35 parts per million (ppm) in HW lignin, indicating the presence of a less rigid aliphatic structure. In contrast, SW lignin has a substantial amount of stiff segments consisting of radically coupled biphenyl and biphenyl ethers based on guaiacylpropane (G) and *p*-hydroxyphenolpropane (H) units (Fig. 2B) formed during the kraft processing (*24*). In addition, the measured ^{13}C-NMR data in the range of 102 to 125 ppm (Fig. 2D) exhibit higher amounts of rigid aromatic methane carbons, $C_{AR\text{-}H}$, presented in SW lignin [195 per 100 aromatic rings (195/100 Ar)] than those presented in HW lignin (185/100 Ar). In HW lignin, both syringyl propane (S) units and syringyl propane with carbonyl at C_α (S′) units (Fig. 2A) contribute to considerable steric hindrance and increased free volume for the lignin molecules, which, in turn, increases the molecular mobility and thus reduces the melt viscosity and glass transition temperature

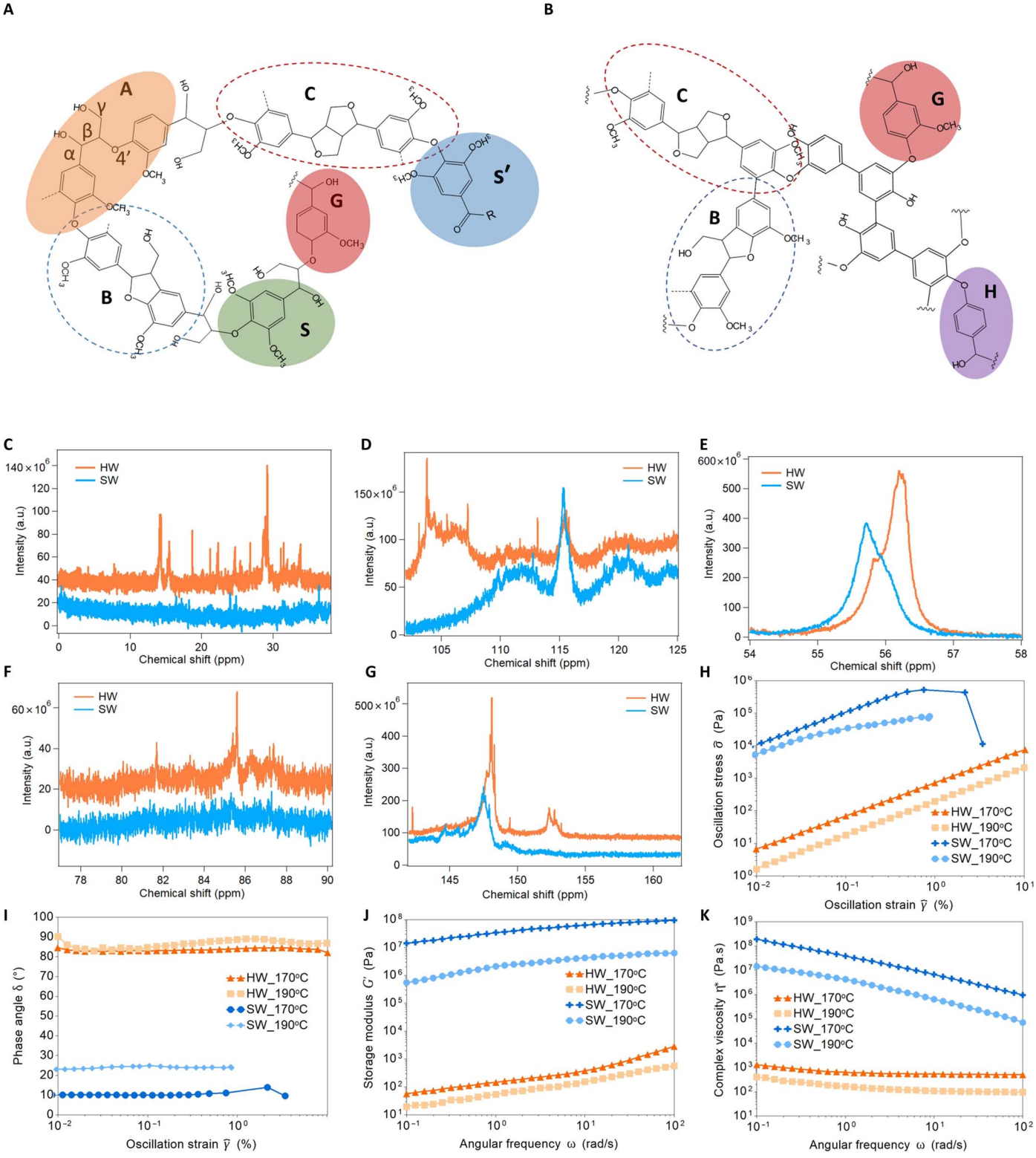

Fig. 2. Structural characteristics and rheological behaviors of two lignins—organosolv HW lignin and a kraft SW lignin. Representative chemical structural units of (**A**) HW lignin and (**B**) SW lignin showing the presence of a flexible ether linkage in the former. The detailed ^{13}C-NMR data of the two lignins: (**C**) aliphatic structure, (**D**) aromatic carbons, (**E**) methoxyl groups, (**F**) ether groups, and (**G**) oxygenated aromatic carbons. Rheological properties of the HW and SW lignins at two reference temperatures including 170° and 190°C: (**H**) shear stress as a function of oscillatory strain and (**I**) their corresponding phase angle characteristics, (**J**) log-log profile of angular frequency dependent dynamic storage moduli, and (**K**) the corresponding complex viscosity as a function of angular frequency. a.u., arbitrary units.

(*25*, *26*). For example, the glass transition temperature (T_g) of HW lignin (ca. 87°C) is almost 100°C lower than the T_g of the kraft SW lignin (ca. 181°C). In addition, in HW lignin, the presence of higher methoxy groups (99/100 Ar versus 68/100 Ar in SW lignin; Fig. 2E), aliphatic ether groups (30/100 Ar versus 17/100 Ar in SW lignin; Fig. 2F), and oxygenated aromatic carbons (236/100 Ar versus 222/100 Ar in SW lignin; Fig. 2G) offers higher degrees of freedom for rotating and bending of molecules (*25*, *26*).

Contrasting structural characteristics of SW and HW lignins (Fig. 2, A and B) based on analysis by NMR support the oscillatory rheology data (Fig. 2H). In the isothermal shear sweep experiments performed at two temperatures (170° and 190°C), the SW lignin exhibits shear-thinning behavior at around 1% strain, whereas the HW lignin exhibits a much longer elastic response, more than 10% strain amplitude. In addition, the determined shear stress of SW lignin in the linear region is more than three orders of magnitude larger than the measured stress of HW lignin. For example, at 190°C and 0.1% strain amplitude, oscillatory stresses of SW lignin and HW lignin are ca. 3.4×10^4 Pa and 18.2 Pa, respectively. The SW lignin presents a strong solid-like behavior, as evident from a very low phase angle (from 10° to 20°) within the investigated temperature range. In contrast, HW lignin revealed liquid-like characteristics with a phase angle approaching 90° (Fig. 2I). The frequency-dependent storage modulus (G') presents a similar trend, in which SW lignin registers G' values that are several orders of magnitude larger than those of the HW lignin (Fig. 2J). Therefore, the complex viscosity of SW lignin is much higher than that of the HW lignin (Fig. 2K). Good flow characteristics are needed for FDM. Our study reveals a very high stiffness of SW lignin in the molten state and a very high resistance to flow (~72,000 Pa·s complex viscosity at 100 rad/s and 190°C) that is not suitable for any melt processing. At room temperature, HW lignin has extraordinary brittleness and stiffness compared to other polymeric materials and a very good flow behavior at processing temperatures (e.g., ~95 Pa·s viscosity at 100 rad/s and 190°C). Thus, the HW lignin exhibits ~3 orders of magnitude reduced viscosity, under identical conditions, compared to that of the SW lignin. Accordingly, an HW lignin macromolecular segment is a better candidate to develop polymeric compositions targeted toward 3D-printing applications. For FDM, both elastomers and semicrystalline polymers are used as printing filaments, in which ABS and nylon are the two most common. Here, we investigate the printability of both cases, HW lignin–based elastomers and HW lignin–based semicrystalline composites. Specifically, HW lignin is incorporated with an NBR41 or nylon 12 for FDM (see tables S1 and S2).

Printability of lignin-based thermoplastic elastomers

In this research, HW lignin was used with a few selected host polymer matrices to obtain 3D-printable and partially renewable soft materials with outstanding flow characteristics. The low viscosity and the low thermal transition temperature of HW lignin were preferred to the characteristics of SW lignin. ABL is a renewable analog of ABS, in which the styrene component of ABS is replaced with lignin in ABL. ABS has a glassy plastic matrix where the rubbery phase is dispersed; in contrast, ABL has a rubbery matrix where the lignin phase is dispersed as discrete domains or as a co-continuous phase (*19*). We synthesized ABL thermoplastic elastomeric compositions based on NBR41 melt mixed with HW lignin using a previously reported protocol (*19*, *20*). Flow characteristics of the composition containing 40, 50, and 60 wt % HW lignin were studied at 230°C, the recommended processing temperature of standard 3D-printable thermoplastic resins such as ABS and HIPS. To avoid accelerated thermal degradation, the operating temperature of HW lignin–containing compositions is recommended to be below 230°C (*20*). The measured complex viscosity data of pristine NBR41 and its ABL compositions as a function of angular frequency at a reference temperature (T_{ref}) of 230°C are presented in Fig. 3A. The viscosity of the NBR41 matrix drops substantially after the addition of the HW lignin. Over a broad range of oscillation frequency, ranging from 0.1 to 10 rad/s, a drop in complex viscosity occurs by approximately an order of magnitude for the NBR41 matrix after incorporation of HW lignin to the matrix by 60 wt % loading. However, the stiffness of the ABL material rises with the increase of lignin loading. For example, the stiffness of the ABL containing 60 wt % HW lignin (as measured by the three-point bending test at T_{ref} = 25°C) exhibits a ca. 5 times higher storage modulus (G') (ca. 163 MPa) than that of the ABL with 40 wt % HW lignin (ca. 34.7 MPa) (see fig. S1A). The improvement of nitrile rubber stiffness at room temperature by adding lignin is expected (*17*, *19*, *20*). The incorporation of a stiffer component (lignin) leads to higher stiffness of nitrile rubber-lignin composites. Lignin does not form a freestanding film due to its very low molecular weight and inherent brittleness; hence, NBR41 is used as a binding segment between lignin molecules. Varying the concentrations of these components results in variable properties of the ABL composites, with increasing lignin content leading to increased brittleness. However, the reduction in the viscosity of ABL melt compared to neat rubber is unique. Good shear-thinning behavior and low viscosity are critical to enhance flow characteristics during the 3D-printing process. Therefore, we targeted 3D printability of the specific ABL composition containing 60 wt % HW lignin.

The measured shear rate–dependent viscosity data are shown in Fig. 3B. In this case, the Cox-Merz rule (*27*) [i.e., $\eta^*(\omega) = \eta(\dot{\gamma})$] was applied to convert the dynamic shear viscosity (η^*) to the steady shear viscosity (η), where ω is the angular frequency and $\dot{\gamma}$ is the steady shear rate. The dynamic frequency sweeps were collected at different temperatures, and time-temperature superposition was used to construct the master curve at a certain reference temperature. By using this method, the storage moduli and complex viscosity as a function of angular frequency and the shift factor a_T were determined. The following Williams-Landel-Ferry (*28*) relationship was used to obtain these master curves

$$\eta = a_T \eta_{ref} \quad (1)$$

and

$$\log(a_T) = -[C_1(T - T_{ref})]/[C_2 + (T - T_{ref})] \quad (2)$$

where η is the viscosity at temperature T, η_{ref} is viscosity at reference temperature T_{ref}, and C_1 and C_2 are the material constants. The flow curves at various temperatures suggest that the ABL sample has a much higher viscosity than the ABS and HIPS samples (Fig. 3B). Both ABS and HIPS reference filaments have good printing characteristics at the recommended temperature range of 230° to 250°C. In addition, the storage modulus (G') plot as a function of angular frequency with a shift factor a_T (Fig. 3C) indicates a good relaxation characteristic for HIPS in the terminal region ($\omega < 0.1$ rad/s) with a slope approaching 2. The ABS sample exhibits a longer relaxation time in comparison to the HIPS filament, as demonstrated by an appreciable decrease in G' with an angular frequency from 0.1 to 0.01 rad/s. In contrast, the ABL sample

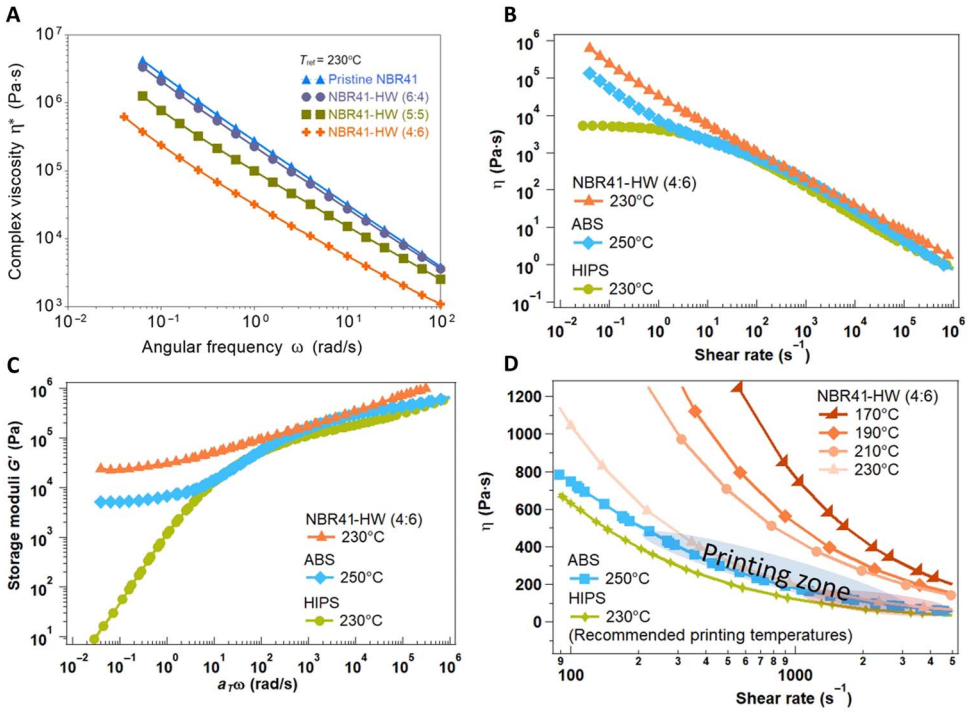

Fig. 3. Rheological properties of NBR41, ABL compositions based on NBR41 containing different HW lignin contents, and two printable polymers—ABS and HIPS—as reference materials. (**A**) Complex viscosity as a function of angular frequency at a reference temperature of 230°C of pristine nitrile-butadiene rubber (41 mol % nitrile) (NBR41) and acrylonitrile-butadiene-lignin (ABL) with 40, 50, and 60 wt % HW lignin contents. (**B**) Viscosity as a function of shear rate at studied reference temperatures of selected ABL (60 wt % HW lignin content), HIPS, and ABS samples (the Cox-Merz rule was applied to convert the complex viscosity to steady shear viscosity). (**C**) Their corresponding master curves, storage moduli as a function of angular frequency, in which a_T is the shift factor obtained from master curve construction. (**D**) Shear rate–dependent viscosity of the selected ABL, ABS, and HIPS samples. Viscosity profiles at recommended temperatures, 250°C for ABS and 230°C for HIPS, were obtained as those exhibit good printing behavior under these conditions. The blue-shaded region presents the viscosity and shear rate window for ABS when it shows good printability. The red-shaded region indicates the overlapped printing viscosity range for ABL, ABS, and HIPS samples.

does not exhibit a notable drop of G' at very low frequency (Fig. 3C). The zero-shear viscosity plateau region is absent in ABL (Fig. 3B). The formation of chemical cross-links and hydrogen bonding between the nitrile rubber and HW lignin can be attributed to the considerably high modulus of ABL at low shear frequency. Only ABS and HIPS samples have a clear plateau modulus region (Fig. 3C) that corresponds to the minima in the tan (δ) profile (see fig. S1B) (*29*). The ABL material has a very low tan (δ) value and the associated low phase angle data (fig. S1C) over the entire angular frequency region ($a_T\omega$). Similarly, the temperature-dependent storage and loss moduli of ABS and HIPS indicate a crossover point at ca. 220°C and ca. 200°C, respectively (fig. S2, A and S2B), whereas the crossover modulus of ABL is not reached even at ca. 220°C (fig. S2C). Consequently, ABL has the lowest temperature-dependent tan (δ) (see fig. S2). The rheological study suggests a very rigid structure and high resistance to the flow characteristics of ABL. The extracted data (Fig. 3D) show a flow property of ABL (with 60 wt % HW lignin) similar to that of the ABS and HIPS at a very high shear rate range, approximately from 1000 to 5000 s^{-1}, which indicates its potential for 3D-printing applications. Recently, Mackay *et al.* (*12*) developed a model to predict the maximum loading velocity of the ABS filament using a dashpot or syringe-piston–type printing device, a LulzBot printer. On the basis of this analysis, the maximum loading speed of ABS at T_{ref} = 250°C is approximately 4.5 mm/s and the minimum velocity of feeding the filament is approximately 0.29 mm/s (*12*).

Our intent is to analyze the printability of the ABL compositions. In addition, we focus on developing other lignin-based compositions and predicting the required characteristics for it to be an excellent printable material. We realize that such a material would have an excellent shear-thinning behavior for ease of melt extrusion but a very high zero-shear viscosity for the required dimensional stability of the melt after it is extruded from the nozzle on a printing bed.

For extrusion through a capillary, the apparent shear rate for a Newtonian fluid is determined by using the volumetric throughput rate that is, again, dependent on the velocity of the solid filament at the entrance of the printer head. The measured logarithmic profiles of viscosity against apparent shear rate give a non-Newtonian shear-thinning index that is used to compute the true shear rate at the printer head nozzle.

The apparent shear rate for a Newtonian fluid can be determined by using Eqs. 3 and 4 (*12*, *30*)

$$\dot{\gamma}_a = 32Q/\pi d^3 \quad (3)$$

$$Q = v_f \pi D_f^2/4 \quad (4)$$

where $\dot{\gamma}_a$ is the apparent shear rate of the polymer melt extruded through the printing nozzle, Q is the volumetric flow rate, d is the diameter of the

printing nozzle, v_f is the filament velocity, and D_f is the diameter of the filament. The computed data for the ABS melt at 250°C are presented in table S3. For a shear-thinning fluid, the true shear rate can be determined by Eq. 5 (*30*)

$$\dot{y}_t = \dot{y}_a(3n+1)/4n \quad (5)$$

where $\dot{y}_t$ is the true shear rate for a non-Newtonian fluid and n is the power law index. The shear stress (σ) at a reference temperature of a shear-thinning fluid is determined by the power law (*12*, *31*)

$$\sigma = K\dot{y}_t^{\,n} \quad (6)$$

where K is the consistency index.

Therefore, the viscosity at a true shear rate can be found by using the following relation

$$\eta = \sigma/\dot{y}_t = K\dot{y}_t^{\,n}/\dot{y}_t = K\dot{y}_t^{\,(n-1)} \quad (7)$$

The consistency index and power law index can be determined from the log-log plot of viscosity as a function of the true shear rate

$$\log(\eta) = \log(K) + (n-1)\log(\dot{y}_t) \quad (8)$$

One may notice that the apparent shear rate determined with a 0.5-mm nozzle diameter varies from 150 to 2400 s^{-1}, which corresponds to a true shear rate ranging from 190 to 3000 s^{-1}. The extracted results from a flow curve of ABS at 250°C suggest a possible viscosity range for 3D printing from ca. 70 to 500 Pa·s (Fig. 3D and table S3). The measured viscosity of ABL shows a good overlapped region with the standard printable resins at shear rates above 1000 s^{-1}, as highlighted by a red-shaded viscosity window in Fig. 3D. Thus, we conclude that 60 wt % HW lignin in nitrile rubber provides good flow characteristics suitable for a 3D-printing process.

For the specific 3D-printing device (Fig. 4) used in this study, the drive wheel that feeds the filament into the heating gun (barrel where the polymer filament melts) during the printing process requires significant force to push the filament out at such a high shear rate. Because of the lack of appropriate stiffness, the ABL filament bends and buckles at such high speed. The digital images shown in Fig. 4 (C and D) are examples of HIPS and ABL filaments. The HIPS filament has a high stiffness, whereas the ABL filament exhibits good flexibility. Examples of the storage moduli as a function of temperature and angular frequency are presented in fig. S3 (A and B), along with the printing process of a HIPS filament in fig. S3E and movie S1. It has been reported that the filament feeding at increased speeds may cause shear failure at the drive wheel (*11*, *12*). For example, the image in fig. S3C presents an ABL filament failure at the contact point with the drive wheel (fig. S3D) at increased feeding speed. This results in the material jamming and halts the melt extrusion through the nozzle, as shown in Fig. 4E. A cause of this failure is ABL's low stiffness, which is illustrated in the measured three-point bending storage modulus data at T_{ref} = 25°C (Fig. 4F). ABL's storage modulus is nearly $^1/_{10}$ that of the ABS and HIPS samples.

This exhaustive study of lignin compounded with NBR to produce ABL revealed shortcomings, i.e., low stiffness and high melt viscosity, prohibiting it from being a candidate for 3D printing. To overcome these challenges, ABL was then alloyed with HIPS in a 50:50 wt % ratio, leading to significantly improved feeding characteristics as shown in fig. S4 (Supplementary Materials). However, mixing lignin with another common 3D-printable polymer, nylon, provides much more promising 3D-printing results. To that end, HW lignin was melt mixed with nylon 12 at 40 to 60 wt % lignin loading, and the resulting three-point bending storage modulus meets the stiffness requirements for rapid filament loading (Fig. 4, F and G). As an added benefit, nylon 12 is an engineering thermoplastic that can also be synthesized from renewables (*32*–*35*); thus, a lignin/nylon 12 alloy has the potential to create a 100% renewable printable product.

Stiffer materials yet better flow properties

The tensile Young's modulus of pristine nylon 12 is only 1.77 ± 0.15 GPa, and the addition of 40 wt % HW in nylon 12 significantly increased the modulus to 3.01 ± 0.59 GPa (approximately 70% increase in tensile Young's modulus), as shown in Fig. 4H (also see fig. S5 and table S4). It is intriguing that the presence of 40 wt % HW lignin also maintains a similar tensile strength with pristine nylon 12, as shown in Fig. 4I. The reinforcement of these composites comes from rigid phenolic units at room temperature. The formation of spherical lignin particles dispersed in the nylon matrix enhanced the mechanical stiffness of the composites. The measured scanning electron microscopy (SEM) images from the three different compositions of HW lignin (40, 50, and 60 wt %) in the nylon 12 matrix are shown in Fig. 5. In these compositions, the diameter of lignin particles varies from ca. 100 nm to ca. 3 μm, and particle size enlarges with increasing lignin content (Fig. 5, A to C). The Lorentz-corrected small-angle neutron scattering (SANS) curves, i.e., Iq^2 versus q, exhibiting correlation peaks in lignin-modified nylon 12 are depicted in Fig. 5D. Incorporation of lignin in the nylon matrix leads to the formation of two correlation peaks, and the associated average correlation distance (L_1 and L_2) between lignin domains in the nylon matrix is calculated by L_1 or $L_2 = 2\pi/q_{max}$. The neutron scattering length density (SLD) of nylon 12 was calculated using a software package developed by the Center for Neutron Research, National Institute of Standards and Technology. The computed SLD of nylon 12 is ca. 0.3×10^{-6} $Å^{-2}$. The SLD of lignin (ca. 1.7 to 1.9×10^{-6} $Å^{-2}$) (*36*) is higher than that of nylon 12. The existing natural SLD contrast allows us to investigate the formation of lignin domains and their correlation length within the nylon 12 matrix without needing deuterated nylon 12. Each sample exhibited two peaks at low and high q, probably due largely to two distributions of characteristic length scales formed between spherical aggregated lignin particles. SANS data obtained from these alloys (see table S5) indicate that L_1 increases with decreasing lignin content, while L_2 remains almost unchanged. We anticipate that the high-q peaks correspond to the average center-to-center correlation distance (L_2, approximately 23 nm) of smaller spherical domains within the composites. The low-q peaks corresponding to the average correlation distance (L_1) between the aggregated larger lignin phases varies from 599 to 837 nm, with decreasing lignin content from 60 to 40 wt %. The SANS results corroborate very well with the collected SEM images shown in Fig. 5 (A to C) (also see fig. S6).

The formation of thermoreversible phase-separated lignin offers interesting properties of the investigated composites. The presence of spherical HW lignin particles with low melt viscosity (see Fig. 2) improved the flow characteristics of nylon 12. Low melt viscosity of HW lignin at high temperatures comes from flexible linkages such as β-O-4′, ether, and aliphatic chains (see the previous discussion).

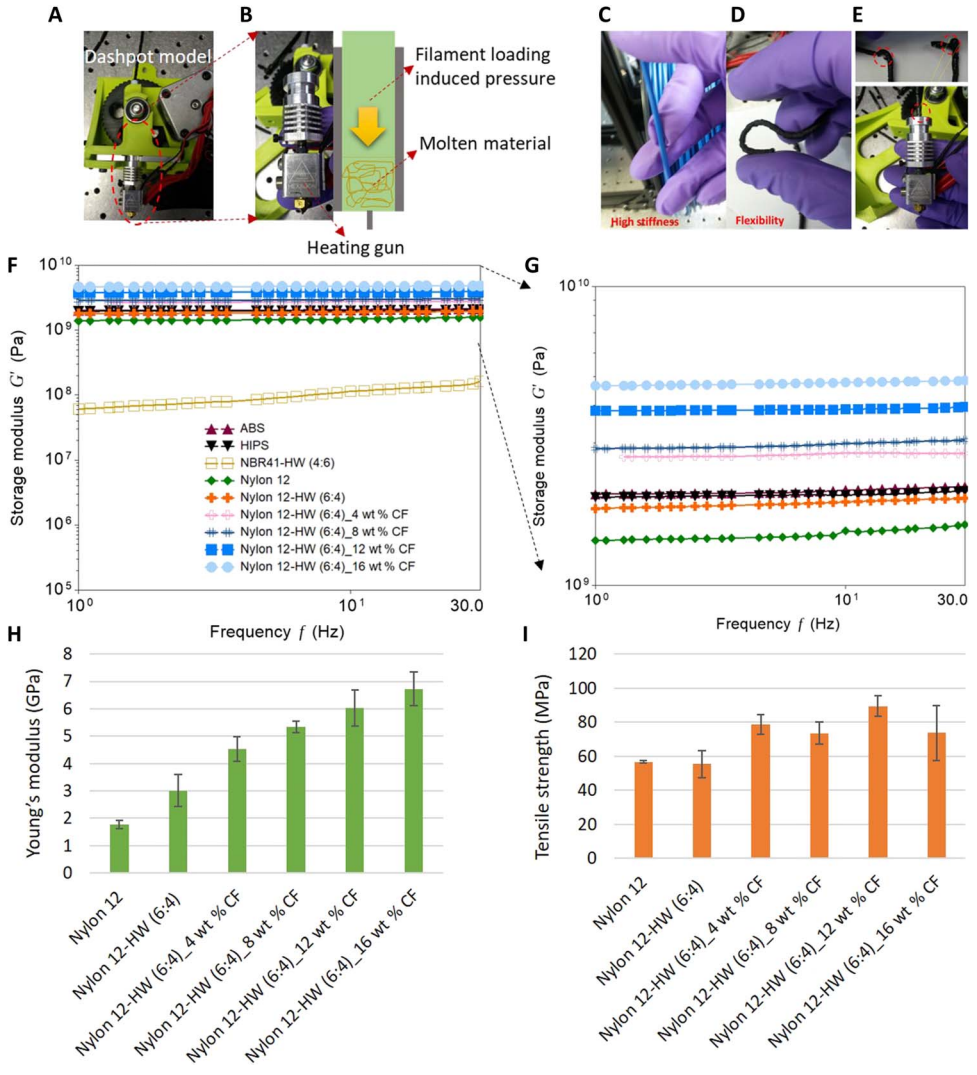

Fig. 4. Melt extrusion of the filament during the printing process and the mechanical properties of lignin-based composites. (**A**) Digital image of a representative printer unit (LulzBot TAZ) used in this study and (**B**) the heating unit. The illustration (right) presents a process of filament loaded into the heating chamber and then melted. The pressure created by the loading filament pushes the molten material extruding through the printer nozzle. (**C**) A digital image of a HIPS filament bent by fingers, indicating high stiffness, and (**D**) a digital image of a 60 wt % HW lignin in NBR41 bent by fingers, indicating a very flexible characteristic. (**E**) Examples of blockages and material jamming during filament loading of the low-stiffness NBR41-HW (60 wt % lignin). (**F**) The measured three-point bending storage modulus (*G′*) as a function of frequency of selected compression-molded samples at 25°C: ABS, HIPS, NBR41–HW lignin (60 wt %), nylon 12, and nylon 12–HW lignin (40 wt %) with different CF contents of 0, 4, 8, 12, and 16 wt %. (**G**) The corresponding zoomed-in three-point bending data with *G′* from 10^9 to 10^{10} Pa for a clear observation. (**H** and **I**) The tensile Young's modulus and tensile strength of selected molded samples.

It is intriguing that the measured rheological results (Fig. 6) indicate a much lower melt viscosity of lignin-modified nylon 12 compared to that of neat nylon 12 and HIPS matrices at T_{ref} = 230°C. At 230°C and in the high–shear rate regime (equivalent to 100 rad/s), nylon 12 has higher melt viscosity (ca. 1050 Pa·s) than HIPS (ca. 630 Pa·s). Thus, the formation of fine spherical lignin particles within the nylon 12 matrix causes a reinforcement effect at room temperature but introduces plasticization in the melt. The significantly low melt viscosity of HW lignin particles, for example, ca. 100 Pa·s at 190°C in the frequency range from 10 to 100 rad/s, causes it to behave like a lubricant phase and mobilizes the nylon macromolecules. Increasing HW lignin content from 40 to 60 wt % further drops the melt viscosity of the nylon 12 significantly (Fig. 6, B to D). For example, at T_{ref} = 230°C and at an angular frequency of 100 rad/s, the complex viscosities of compositions containing 40, 50, and 60 wt % HW lignin are ca. 150, 91, and 32 Pa·s, respectively. Thus, nylon 12–HW lignin alloys reveal good flow characteristics that match the required viscosity and shear rate windows for 3D printing. The addition of rigid and high–aspect ratio fillers, such as CFs that do not melt in polymers, significantly improves the polymer mechanical properties but usually increases the melt viscosities of the composites. In this study, the HW lignin filler demonstrates contradictory characteristics; for example, it is stiffer at room temperature yet flows better in the melt.

During the 3D-printing process, the molten material is extruded and deposited layer by layer at a high shear rate. The shear rate applied on the newly printed layer is significantly reduced (approaching zero shear) after deposition. Therefore, it requires a relatively high melt modulus to maintain the 3D shape of the printed object. In addition, the large

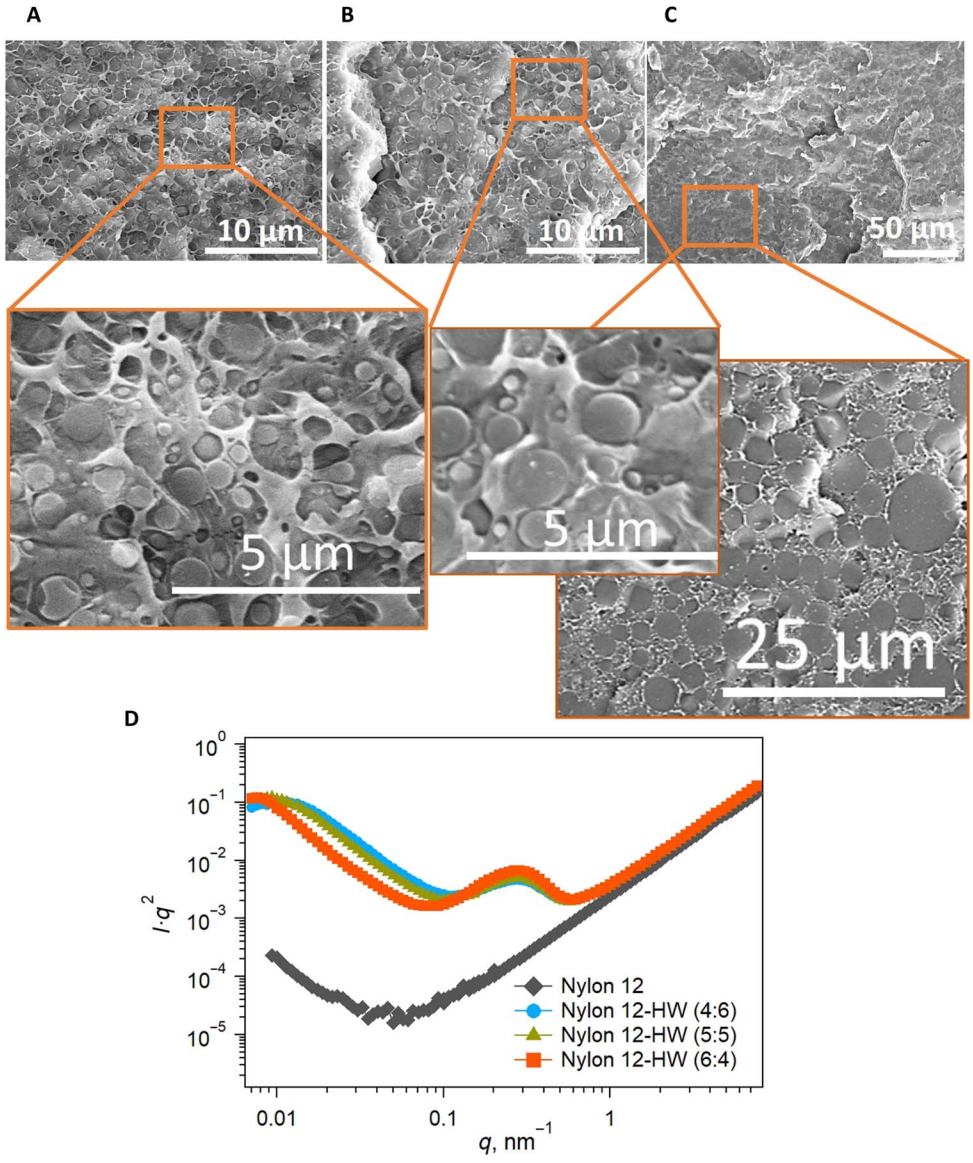

Fig. 5. Morphological properties of nylon 12 and nylon 12–HW lignin composites. The scanning electron micrographs of different HW lignin–based nylon 12 composites: (**A**) 40 wt % lignin, (**B**) 50 wt % lignin, and (**C**) 60 wt % lignin. (**D**) Lorentz-corrected SANS data of the corresponding lignin-modified nylon 12 samples.

deformation caused by the movement of the printer nozzle and high melt extruding flow right after depositing the material requires the molten polymer to have high yield stress to stabilize the printed shape. The principle of liquid-like materials such as colloidal gels and hydrogel extrusion was additionally used in 3D-printing technology; in this case, the viscoelastic response of the gel-like materials is critical. The materials must have high shear-thinning behavior and should retain the 3D structure after deposition. Therefore, for good printability, a processing window is defined: Viscosity should be between 20 and 280 Pa·s, modulus should range from 10^3 to 10^5 Pa, and yield stress should have a value from ca. 150 to 10^3 Pa (*6*, *37*–*43*). In this study, both the storage modulus and yield stress of these nylon/lignin composite melts are within the range of ca. 10^3 to 10^5 Pa, which are comparable to the required yield stress and the storage modulus to maintain good dimensional stability after deposition (see the data in figs. S7 and S8). Filaments extruded from the lignin-based materials have sufficient flexibility to be rolled and loaded in a 3D printer. This flexibility depends on the lignin content in which decreasing lignin content increases flexibility. An example of a rolled filament made from 40 wt % HW lignin in nylon 12 is presented in fig. S4F. The digital images shown in Fig. 6G are examples of 3D-printed objects made from nylon 12 containing 40 wt % HW lignin (black color) and HIPS (blue color). A video of an oak leaf printing process is available in movie S5.

To enhance the stiffness of the material further and to facilitate uninterrupted high-speed feeding of filaments, we incorporated chopped CFs in the nylon 12–HW lignin blends. Utilization of CFs in the lignin-modified nylon matrix improves the mechanical properties of the material without affecting 3D printability. For example, lignin-modified nylon composites containing up to 16 wt % CF exhibit viscosities at high shear rates that are lower than that of the neat nylon

matrix (Fig. 6E). At high frequency, above 10 rad/s, the viscosity of these composites is considerably lower than that of the reference filament, HIPS. For example, at 100 rad/s, the viscosities of lignin (40 wt %)–loaded nylon 12 melt containing 4, 8, 12, and 16 wt % CF are 266, 420, 442, and 630 Pa·s, respectively. All these composite samples reveal good shear-thinning characteristics, and the flow curves fall within the printing zone, as analyzed and discussed earlier. Moreover, the data in Fig. 4 (F to I) (also see fig. S5 and table S4) demonstrate the effect of CFs on the improvement of mechanical performance of the lignin-based nylon 12 composites. For example, a 12 wt % CF-containing polymer matrix made of nylon 12–HW lignin (6:4) alloy shows >80 MPa tensile strength and ca. 6 GPa tensile modulus (Fig. 4, H

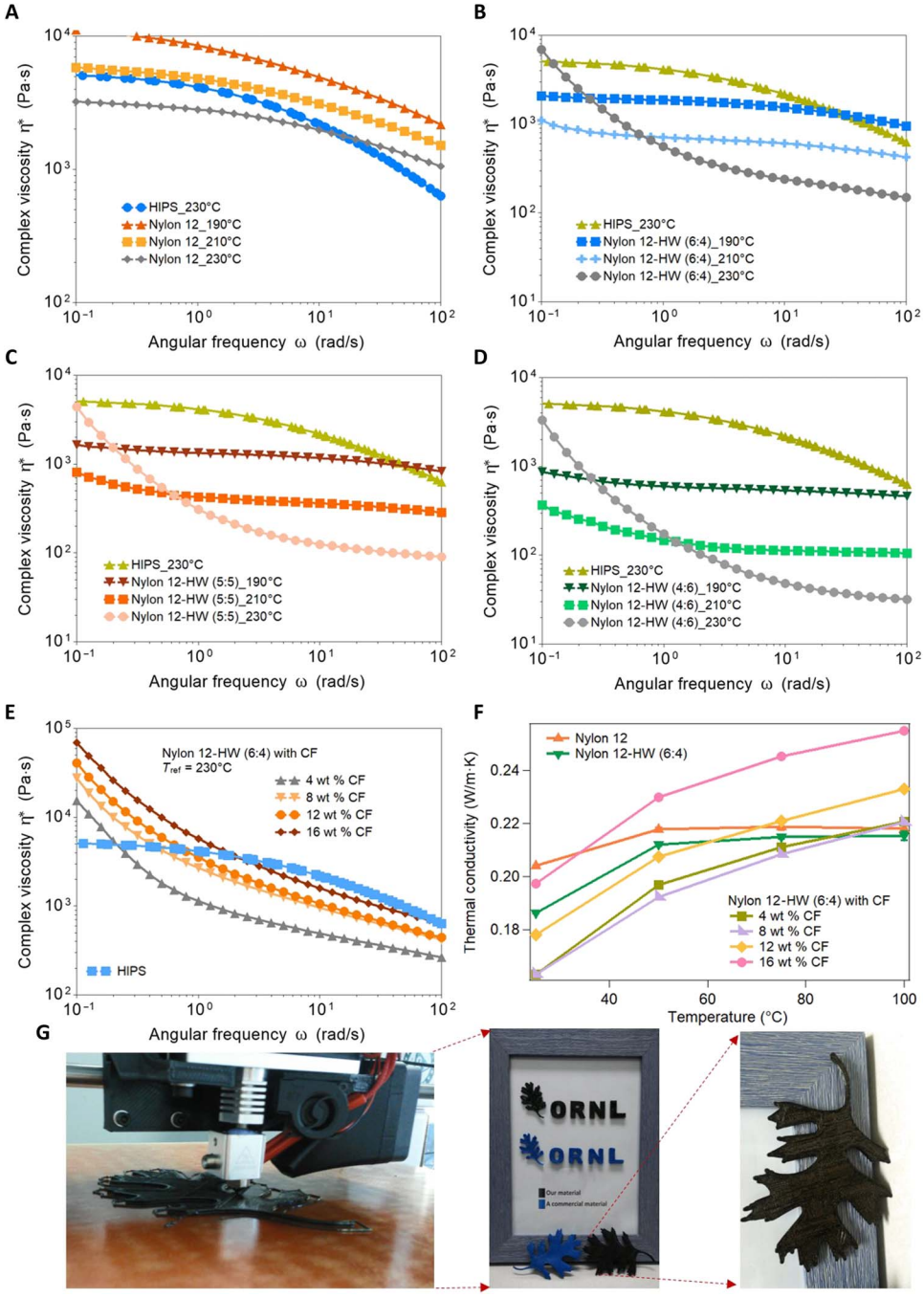

Fig. 6. Complex viscosity of HIPS, nylon, and its composites with different HW contents. (**A**) HIPS and nylon 12, (**B**) HIPS and nylon 12 with 40 wt % HW, (**C**) HIPS and nylon 12 with 50 wt % HW, and (**D**) HIPS and nylon 12 with 60 wt % HW samples. (**E**) Complex viscosity at a reference temperature of 230°C of HIPS and HW–nylon 12 (40 wt % HW) with different CF contents (from 4 to 16 wt % CF). (**F**) Thermal conductivity as a function of temperature of nylon 12, nylon 12–HW (40 wt % lignin), and composites of nylon 12–HW (40 wt % lignin) with varied CF contents. (**G**) Digital images of a printing process of nylon 12–HW (40 wt % lignin) and its printed oak leaf and ORNL (black) in comparison with printed ones made from HIPS (blue) material for reference.

and I, and table S4). In addition, the three-point bending storage moduli (G') increased drastically with the incorporation of lignin and CFs to the pristine nylon 12. For example, G' of pristine nylon 12 at 25°C and 30 Hz is ca. 1.59 GPa. Under identical conditions, the alloy of nylon 12 with 40 wt % HW lignin has a modulus of ca. 1.96 GPa. However, by adding only 4 wt % CF and 16 wt % CF in the nylon 12–HW lignin alloy, the modulus increases to ca. 2.76 GPa (increasing ~41%) and 4.84 GPa (increasing ~147%), respectively (see Fig. 4, F and G). The SEM images reveal good dispersion of CFs within the polymer matrix. The formation of spherical aggregated lignin phases within the nylon 12 matrix in the presence of CFs was also observed, as shown in the high-resolution SEM images (see fig. S9). The increase in material stiffness without a dramatic increase in the viscosity profile by the addition of CF facilitates increased feeding speed during the printing process of nylon 12 renewable composites.

Rapid melting of the polymer is critical to maintain steady-state filament feeding and extrusion rates through the 3D-printing nozzle. Therefore, efficient heat transfer from the heating gun's wall to the bulk filament is needed (*11*). This is achieved by loading CFs into the filament, which reduces the radial temperature gradient. Thermoplastic polymers have a very low thermal conductivity. Therefore, the heat transfer from the wall of the heating gun to the center of the loaded filament is slow. The measured thermal conductivity of nylon 12 and nylon 12 containing 40 wt % HW lignin samples is almost identical at a broad temperature ranging from 50° to 100°C (Fig. 6F and table S6). For example, the thermal conductivity at 100°C of nylon 12 and its composite with 40 wt % HW lignin is 0.2181 ± 0.0025 W/m·K and 0.2154 ± 0.0017 W/m·K, respectively. The addition of CFs into the lignin-loaded nylon causes a temperature-dependent thermal conductivity trend. With higher CF contents of 12 and 16 wt % fiber loading, the thermal conductivity of the composite increases to 0.2331 ± 0.0006 W/m·K (10% increase) and to 0.2551 ± 0.0004 W/m·K (24% increase), respectively. The enhancement of thermal conductivity at high temperatures increases the heat transfer from the heating gun to the material and reduces the phase transition time from solid to liquid. In addition, after extruding and stacking layers of the printed molten material, the material solidifies faster and fixes the 3D shape quickly without deformation when thermal conductivity of the material is high. The presence of fiber reinforcement resists deformation due to the shrinkage force experienced by relaxation of the oriented molecules that are rapidly laid through a small nozzle. Thus, the presence of fibers is expected to enhance dimensional stability during printing of composite materials.

The printed objects using the lignin-modified nylon 12 material exhibit good performance, comparable to a standard HIPS commercial filament. Two selected lignin-based composites were used to prepare dog-bone samples (see fig. S10A) for mechanical performance analysis (fig. S10, B to D). The measured tensile data of the 3D-printed, lignin-modified nylon and its fiber-reinforced composite samples indicate equivalent mechanical stiffness to that of the corresponding compression-molded samples (see Figs. 4H and 7A). For example, the tensile Young's moduli of molded nylon 12–HW lignin (40 wt %) with 4 wt % CFs and the corresponding printed bar are 4.52 ± 0.45 GPa and 4.49 ± 0.74 GPa (table S7), respectively. The low melt viscosities of these samples (see Fig. 6, B and E) allow good diffusion at the interface of printed layers, leading to elimination of porosity in the printed mass (shown in Fig. 7, B and C). Like common printed objects made from viscous melts of commodity polymers, the printed HIPS sample cross section exhibits presence of pores between layers. High resistance to flow of HIPS prevents molecular diffusion at the interface of printed layers (as shown in Fig. 7D).

We anticipated a significant influence of lignin and CFs on the morphology of the 3D-printed nylon 12 matrix; in addition, the printing flow may also contribute to the morphology of the materials. The measured 2D x-ray diffraction (2D-XRD) data show a diffraction peak at $q \sim 12.8$ (nm^{-1}) with a d-spacing of ca. 0.41 nm (Fig. 7E), indicating the presence of a γ-phase, hexagonal structure (*44*–*47*). It is apparent that the unit cell structure remains unaltered as the diffraction peaks do not shift in the presence of HW lignin and CFs. Neat nylon 12 exhibits four sharp diffraction peaks at $q \sim 3.3$, 6.6, 12.8, and 22.7 (nm^{-1}), whereas the lignin and CF-filled samples indicate less intense and broad peaks. These data reveal higher crystallinity and a more perfect crystal structure in the neat nylon 12 sample in comparison with the composites with HW lignin and CFs (*48*). The measured 2D-XRD results are consistent with the calorimetry data (shown in Fig. 7, F and G) (also see fig. S10, H and I, and table S8). The presence of lignin and CF inhibits crystallization kinetics of nylon 12 and causes imperfect crystal formation that leads to a lower melting temperature. For example, both nylon 12–HW (6:4) and nylon 12–HW (6:4) with 4 wt % CF indicate a melting temperature at ca. 170°C, whereas neat nylon 12 has a sharp melting peak at ca. 175°C (Fig. 7F). Nonisothermal crystallization of nylon 12 has been carried out by cooling from the melt, 230° to −80°C, at 10°C/min (see Fig. 7G). Neat nylon 12 recrystallizes at a higher temperature (ca. 154.6°C) in comparison to nylon 12–HW (6:4) (ca. 138.3°C) and nylon 12–HW (6:4) with 4 wt % CF (ca. 140.4°C). The presence of CFs (from 4 to 16 wt % content) indicates a slightly higher recrystallization temperature (T_{rec}) than that of nylon 12–HW lignin composites (see Fig. 7G, fig. S10H, and table S8). The integrated area under the recrystallization peak after normalization, with respect to the weight fraction of nylon 12 in the composites, has been used to determine the enthalpy of recrystallization, ΔH_{rec}, (see table S8). In all cases, neat nylon 12 indicates a higher ΔH_{rec} (ca. 73.2 J/g) in comparison to nylon 12–HW lignin (6:4) with CFs. For example, the nylon 12–HW lignin (6:4) with 16 wt % CFs exhibits $\Delta H_{rec} \sim 66.3$ J/g. The effect of HW lignin on nylon 12 recrystallization is also visible with the significant drop of the T_{rec}, with increasing HW lignin content from 40 to 60 wt % (fig. S10I). An approximately 40°C decrease in T_{rec} of the nylon 12 matrix occurs in the presence of 60 wt % HW lignin. The presence of CFs and HW lignin within nylon 12 not only reduces the matrix melting point but also significantly enhances the melt-flow characteristics. In addition, slow crystallization of nylon 12 in a wide range of temperatures allows favorable welding and fusion characteristics of the layers during printing.

The relative effect of flow and Brownian motion on CFs suspended in the melt can be determined by using the Peclet number (*Pe*) (*49*)

$$Pe = l^2\dot{\gamma}/D \tag{9}$$

where $D = K_B T/6\pi\eta l$ is the diffusion coefficient (K_B is the Boltzmann's constant, T is the printing temperature, and η is the melt viscosity of the composite), l is the CF length, and $\dot{\gamma}$ is the shear rate. CFs have a very high aspect ratio with diameters of approximately 7 μm (see fig. S9) and lengths on the order of centimeters (1/8 inch). By computing the *Pe* at the shear rate of 100 s^{-1} with a corresponding viscosity of ca. 266 Pa·s and a T_{ref} = 230°C, we find *Pe* to be extremely large, approximately 2.3×10^{17}, suggesting the domination of flow over randomization of CF orientation. The alignment of CFs in the printed composites is visible in the SEM images (shown in Fig. 7, H and I). The cross-sectional SEM image (Fig. 7I) exhibits individual CFs aligned perpendicular to the viewing plane. In addition, clear alignment of CFs along the printing

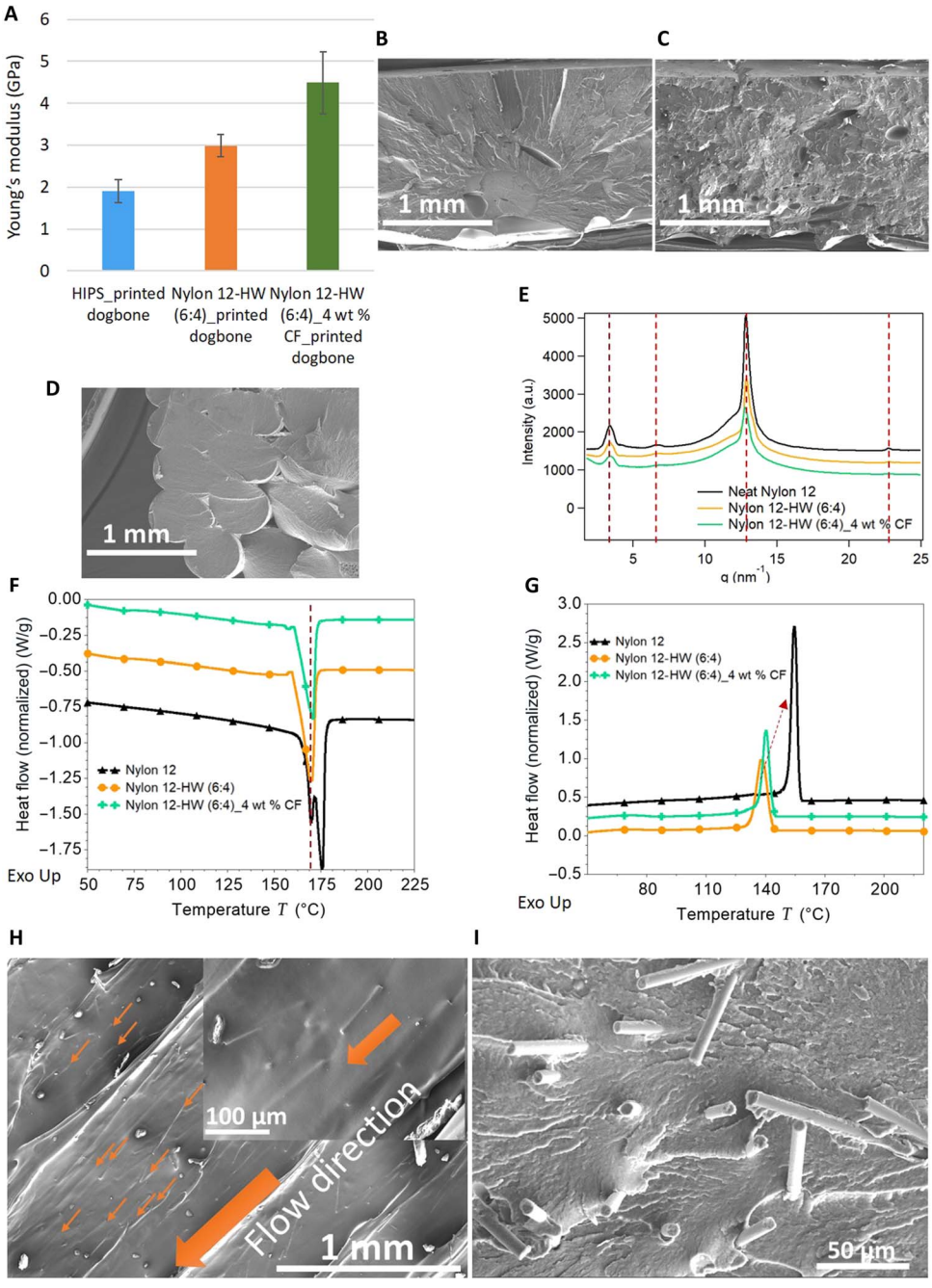

Fig. 7. Crystallization of nylon 12 in the presence of lignin and CFs and mechanical performance of 3D-printed dog-bone samples. (**A**) The measured tensile Young's modulus of 3D-printed dog-bone samples of HIPS, nylon 12–HW (40 wt % lignin), and nylon 12–HW (40 wt % lignin) with 4 wt % CFs. The measured SEM images of corresponding dog-bone samples: (**B**) nylon 12–HW (40 wt % lignin), (**C**) nylon 12–HW (40 wt % lignin) with 4 wt % CFs, and (**D**) HIPS. (**E**) The measured 2D-XRD patterns. (**F**) The measured differential scanning calorimetry (DSC) heating curves and (**G**) the DSC cooling curves of selected samples, including neat nylon 12, nylon 12–HW (40 wt % lignin), and nylon 12–HW (40 wt % lignin) with 4 wt % CFs. Alignment of CFs along the 3D-printing flow direction: (**H**) top view and (**I**) cross section.

flow direction was confirmed in the top-view SEM image (shown in Fig. 7H, marked by the orange arrows). The presence of long CFs within the composite is bound to create rough 3D-printed surfaces (Fig. 7H) and misaligned CFs along the printing flow direction (Fig. 7I). These features, however, help to enhance the adhesion between the 3D-printed layers. Several studies reported the use of CFs to enhance interlayer welding energies during 3D printing of composites (*23*, *50*).

Concluding remarks

We measured the rheological properties of two lignins, an organosolv fractionated HW lignin and a kraft SW lignin, and correlated them to their molecular architectures. The dominance of β-O-4′ linkages, aliphatic segments, aliphatic ether groups, and oxygenated aromatic carbons in sinapyl alcohol–rich HW lignin offers good thermal processing characteristics. In contrast, kraft SW lignin has significant amounts

of stiff segments consisting of radically coupled biphenyl and biphenyl ethers based on G and H units, and this leads to it having a high softening point and higher viscosity. We have successfully defined a viscosity window, from ca. 70 to 500 Pa·s, for good printability via melt extrusion–based 3D printing of lignin-based materials. The characteristics of different HW lignin compositions analogous to the most common polymer 3D-printing materials, ABS and nylon, were compared to evaluate their printability. ABS was modified through substituting lignin with styrene by mixing lignin with nitrile-butadiene rubber to form ABL, and nylon was modified by simply blending it with lignin. While ABL revealed properties that were not conducive for 3D printing, lignin/nylon blends demonstrated promising properties for 3D printability. This allowed lignin to be used as a renewable feedstock to develop green materials for 3D-printing applications. The rheological properties and their correlated chemical structures helped us design and prepare renewable polymeric compositions for 3D printing. HW lignin reinforced the thermoplastic matrix (nylon 12) at room temperature, increasing the stiffness of the mixture, yet also reducing its melt viscosity, leading to outstanding 3D printability. These characteristics were likely due to the formation of phase-separated lignin domains having good thermoreversible hydrogen-bonding interactions with the matrix. The addition of CFs increased the temperature-dependent thermal conductivity of the renewable 3D-printing materials. Improved thermal conductivity of our new environmentally friendly 3D-printing material adds potential tunability of heat transfer via CF concentration and fiber alignment. In addition, the presence of CFs increased the material's stiffness and strength, thus dramatically improving the material throughput rate. For example, the presence of only 12 wt % CF in nylon 12–HW lignin (6:4) resulted in significantly higher tensile strength (over 80 MPa) and a tensile modulus (ca. 6 GPa), over three times higher than the tensile modulus of nylon 12 (ca. 1.77 GPa). Alignment of high aspect ratio fillers by the printing flow suggests a feasible technique to develop printed objects having anisotropic properties for specific applications such as unidirectional heat transfer and directionally reinforced structures.

We find that microscale dispersion of spherical HW-lignin particles within the nylon 12 matrix caused an increase in the particle size with increasing lignin content. The presence of two characteristic length scales between the aggregated lignin domains was identified by SANS in combination with scanning electron microscopy. The low melt viscosity of these dispersed HW-lignin particles improves the flow characteristics of nylon 12. Our continued investigation focuses on further disintegration of these particle clusters, which may improve the material's performance in the future. Moreover, we found that the presence of CFs and lignin led to a significant decrease in the melting temperature and recrystallization temperature of nylon 12, which leads to low-melting imperfect crystals. For example, a ~40°C decrease in recrystallization temperature of nylon 12 occurred in the composite having 60 wt % HW lignin. Low melting and recrystallization temperatures offer better printability at a lower temperature without degrading the lignin. In addition, reducing the viscosity within the composites allows excellent interlayer fusion in high-performance printed objects.

The current market for materials used in the melt extrusion–based printing technique is immense. However, petroleum-based thermoplastics dominate this market. The market for wood and plant-based materials used in this 3D-printing technology is limited because of their inherent difficulties in melt processing. Our study opens a new avenue of using isolated lignin as a feedstock for formulating 3D-printing materials having superior mechanical and printing characteristics. Our findings have the potential to create additional revenue streams for biomass processing industries via the added value of lignin. In addition, it may accelerate installation of pilot biomass fractionation units in rural areas before feeding the whole biomass to a biorefinery and boost local polymer compounding industries that manufacture or compound materials for 3D printing and injection molding.

MATERIALS AND METHODS

Materials

Two selected lignins including kraft SW and organosolv HW were obtained from Domtar, North Carolina, and Lignol Innovations, Canada. NBR41 and nylon 12 were purchased from Scientific Polymer. Discontinuous PAN-based CFs of 1/8-inch length without any applied sizing were provided by E&L Enterprises Inc., Tennessee. Two selected 3D-printing filaments including ABS and HIPS were purchased from LulzBot, USA.

Composite synthesis

NBR41 and HW lignin were blended at an elevated temperature (180°C) with different weight ratios including 40, 50, and 60 wt % HW contents. A Brabender Plasti-Corder Torque Rheometer fitted with a half-size (30 cm^3) mixing chamber and high-shear twin roller blades were used for the melt mixing of rubber and lignin. First, the nitrile rubber was loaded into the mixing chamber to premelt at 90 rpm for 2 min. Then HW lignin was slowly added for mixing for a total of 60 min. The mixed samples were stored at room temperature before pressing to make films for characterization. A hydraulic Carver press was used to press the composites at 190°C and 4 metric tons for 20 min. Similarly, nylon 12 was premelted and mixed at 190°C and 90 rpm for 5 min. Then, HW lignin was slowly added and mixed for a total of 15 min. The HW lignin content varied from 40 to 60 wt %. A composition of 40 wt % HW in nylon 12 was selected to prepare the composites with CF. After mixing HW lignin and nylon 12 for 15 min, CFs were added and mixed for a total of 30 min. The CF content ranges from 4 to 16 wt %. The samples were hot pressed at 190°C for 10 min for characterization.

Rheological measurements

A Discovery Hybrid Rheometer (DHR-3, TA Instruments) was used to investigate the rheological properties of the lignin-based composites. Parallel plates 8 mm in diameter with a sample gap of approximately 0.4 mm were used for all the melt rheological characterizations. Strain sweeps at 100 rad/s and selected temperatures ranging from 170° to 230°C were carried out to determine the elastic response of the studied samples in the melt. Frequency sweeps from 100 to 0.1 rad/s at different temperatures were performed, and the master curves were constructed. The measurements were carried out in the linear regions (very low strain) and in a nitrogen atmosphere.

Mechanical measurements

Dynamic mechanical analysis (DMA) was carried out using a DMA-Q800 (TA Instruments). The three-point bending characterization using a dual cantilever was used. Samples of ca. 1.5 mm by 10 mm by 60 mm were prepared for the DMA measurements. The frequency sweeps at small strain amplitude, 0.1% strain, and 25°C were conducted. The measured tensile data were collected using an MTS Twin-Screw Tensile Tester fitted with a 2000-N load cell. Samples with a ca. 0.5- to

1-mm thickness were cut into dumbbells using a QualiTest ASTM D-638-5-IMP die and tested at a strain rate of 1 mm/min. The measured mechanical data are the averages of six individual measurements.

Small-angle neutron scattering

SANS measurements were performed at the general-purpose SANS (CG2) beamline of the high-flux isotope reactor at the Oak Ridge National Laboratory (ORNL). To cover the q range of interest, two SANS configurations with different neutron wavelengths/sample-to-detector distances, i.e., 4.75 Å/4.9 m and 12 Å/19.4 m, were chosen. Here, q is the magnitude of the scattering vector defined as $q = |q| = 4\pi\lambda^{-1}\sin\theta$, with λ and θ being the wavelength of the incident neutron beam and half of the scattering angle, respectively. Scattered neutrons were collected using a 2D position sensitive ^{3}He detector with a 1 m by 1 m active area, composed of tube detectors providing 256 × 192 pixels. The composite samples were loaded onto 1-mm-thick quartz disks, and the scattered beam was collected at each SANS configuration. The raw 2D SANS data were corrected for detector response, dark current, and scattering from solvents and background before being azimuthally averaged to produce the 1D SANS profiles, i.e., $I(q)$ versus q profile. The data were placed on an absolute scale (cm^{-1}) using a measured direct beam.

SEM measurements

Liquid nitrogen was used to fracture the studied samples. The fractured surfaces were investigated by SEM using the Hitachi S-4800 field-emission scanning electron microscope at different magnifications. An accelerating voltage of 10 kV and a working distance of ca. 9 to 10 mm were applied.

Thermal analysis

Thermal transition temperatures and melting characteristics of nylon 12, nylon 12–HW lignin composites, and composites of nylon 12–HW (6:4) with different CF contents were measured by using a differential scanning calorimeter (Q2000, TA Instruments). Hermetic pans were used for all measurements. Three cycles of heating and cooling (from −80° to 230°C), a ramp rate of 10°C/min, and a sample weight of ca. 4 mg were used. The second heating and cooling cycles were used to determine the melting and recrystallizing temperatures of the investigated samples. The second and third cycle data appear identical. Integration of the area under the recrystallization peak was used to study the enthalpy of the recrystallization process of neat nylon 12 and nylon 12 in the presence of HW lignin and CFs. All the enthalpy measurements were normalized with the corresponding weight fraction of nylon 12 in these composites.

Thermal conductivity measurements

Selected samples of ca. 1.5-mm thickness and ca. 50-mm diameter were used for thermal conductivity measurements using a Fox-50 thermal conductivity meter (TA Instruments). Measurements were made at four different temperatures: 25°, 50°, 75°, and 100°C. The measured data at each temperature were collected by averaging 10 different measurements. A 5°C temperature difference between the lower and the upper temperature was applied to investigate thermal diffusivity. WinTherm-50 software was used to analyze the data.

2D-XRD measurements

The crystal structure of selected samples of nylon 12 with HW lignin and CF composites was determined by a high-intensity microfocus rotating anode x-ray generator (MicroMax-007HF, Rigaku). The following were applied for all measurements: voltage, 40 kV; current, 30 mA; distance, 100 mm; frame width, 0.1 mm; wavelength, 1.54178 Å; and exposure time, 180 s.

Printing process

Filaments of selected composites of NBR41–60 wt % HW lignin and 40 wt % HW lignin in nylon 12 were extruded at 210°C using a custom-designed single-shot extruder equipped with a single die. The filament diameter is ca. 2.5 mm. The materials were 3D printed on a LulzBot TAZ printer equipped with a 0.5-mm-diameter nozzle. The printing and the bed temperatures for HIPS and lignin-based composites are 230° and 100°C, respectively. All samples were 3D printed, with the same printing protocol for comparison. The Cura-LulzBot software was used to control the printing process.

SUPPLEMENTARY MATERIALS

Supplementary material for this article is available at http://advances.sciencemag.org/cgi/content/full/4/12/eaat4967/DC1

Fig. S1. Mechanical properties of NBR41–HW lignin composites and rheological characteristics of ABS, HIPS, and the NBR41–HW lignin composite.
Fig. S2. Temperature-dependent storage modulus (G'), loss modulus (G''), and tan δ of selected samples.
Fig. S3. Rheological data of HIPS and NBR41-HW (60 wt % lignin) at selected 3D-printing temperatures and filament-loading failure.
Fig. S4. Digital images of extruded 3D-printing filaments and 3D-printed objects.
Fig. S5. Mechanical data of nylon 12 and the composites of nylon 12 with different lignin and CF compositions.
Fig. S6. Morphological characteristics of nylon 12 and nylon 12–HW lignin composites.
Fig. S7. Rheological characteristics of ABS, HIPS, and the NBR41–HW lignin composite.
Fig. S8. Rheological data of nylon 12 and the composites of nylon 12 with different lignin and CF compositions.
Fig. S9. Morphological characteristics of nylon 12–HW composites containing CFs.
Fig. S10. The measured mechanical properties, crystal structure, and differential scanning calorimetry of selected samples.
Table S1. Compositions of lignin with NBR41 and nylon 12.
Table S2. Composites of nylon 12–HW lignin (6:4, 40 wt % lignin) with CFs.
Table S3. Shear rate and viscosity window for good printability.
Table S4. The measured mechanical properties of nylon 12 and the mixtures with different HW lignin and CF contents.
Table S5. Correlation lengths in lignin-modified nylon 12 matrices based on Lorentz-corrected SANS data.
Table S6. Thermal conductivity at selected temperatures of nylon 12, nylon 12–HW (40 wt % lignin), and composites of nylon 12–HW (40 wt % lignin) with different CF content, from 4 wt % CF to 16 wt % CF.
Table S7. The measured mechanical properties of selected 3D-printed dog-bone samples.
Table S8. The measured recrystallization temperature (T_{rec}) and enthalpy of recrystallization (ΔH_{rec}) (the integrated area under the recrystallization peak) of selected samples.
Movie S1. An example of a 3D-printing process using HIPS filament.
Movie S2. An example of extruding a molten composite of 50 wt % NBR41-HW (60 wt % lignin) with 50 wt % HIPS.
Movie S3. An example of a 3D-printing process using a composite of 50 wt % NBR41-HW (60 wt % lignin) mixed with 50 wt % HIPS filament.
Movie S4. An example of extruding a molten renewable composite of nylon 12–HW (40 wt % lignin).
Movie S5. An example of 3D printing an oak leaf using the renewable composite of nylon 12–HW (40 wt % lignin).
Movie S6. An example of 3D printing a gear using the renewable composite of nylon 12–HW (50 wt % lignin).
Movie S7. An example of the 3D-printing process of a dog-bone sample using the renewable composite of nylon 12–HW (40 wt % lignin) with 4 wt % CFs.

REFERENCES AND NOTES

1. Z. Quan, A. Wu, M. Keefe, X. Qin, J. Yu, J. Suhr, J.-H. Byun, B.-S. Kim, T.-W. Chou, Additive manufacturing of multi-directional preforms for composites: Opportunities and challenges. *Mater. Today* **18**, 503–512 (2015).

2. S. A. M. Tofail, E. P. Koumoulos, A. Bandyopadhyay, S. Bose, L. O'Donoghue, C. Charitidis, Additive manufacturing: Scientific and technological challenges, market uptake and opportunities. *Mater. Today* **21**, 22–37 (2017).
3. S. Miao, N. Castro, M. Nowicki, L. Xia, H. Cui, X. Zhou, W. Zhu, S.-J. Lee, K. Sarkar, G. Vozzi, 4D printing of polymeric materials for tissue and organ regeneration. *Mater. Today* **20**, 577–591 (2017).
4. H.-W. Kang, S. J. Lee, I. K. Ko, C. Kengla, J. J. Yoo, A. Atala, A 3D bioprinting system to produce human-scale tissue constructs with structural integrity. *Nat. Biotechnol.* **34**, 312–319 (2016).
5. J. U. Lind, T. A. Busbee, A. D. Valentine, F. S. Pasqualini, H. Yuan, M. Yadid, S.-J. Park, A. Kotikian, A. P. Nesmith, P. H. Campbell, J. J. Vlassak, J. A. Lewis, K. K. Parker, Instrumented cardiac microphysiological devices via multimaterial three-dimensional printing. *Nat. Mater.* **16**, 303–308 (2017).
6. A. S. Gladman, E. A. Matsumoto, R. G. Nuzzo, L. Mahadevan, J. A. Lewis, Biomimetic 4D printing. *Nat. Mater.* **15**, 413–418 (2016).
7. X. Wang, M. Jiang, Z. Zhou, J. Gou, D. Hui, 3D printing of polymer matrix composites: A review and prospective. *Composites Part B* **110**, 442–458 (2017).
8. P. Wu, J. Wang, X. Wang, A critical review of the use of 3-D printing in the construction industry. *Autom. Construct.* **68**, 21–31 (2016).
9. U. Kalsoom, P. N. Nesterenko, B. Paull, Recent developments in 3D printable composite materials. *RSC Adv.* **6**, 60355–60371 (2016).
10. J. Zhang, X. Feng, H. Patil, R. V. Tiwari, M. A. Repka, Coupling 3D printing with hot-melt extrusion to produce controlled-release tablets. *Int. J. Pharm.* **519**, 186–197 (2017).
11. J. Go, S. N. Schiffres, A. G. Stevens, A. J. Hart, Rate limits of additive manufacturing by fused filament fabrication and guidelines for high-throughput system design. *Addit. Manuf.* **16**, 1–11 (2017).
12. M. E. Mackay, Z. R. Swain, C. R. Banbury, D. D. Phan, D. A. Edwards, The performance of the hot end in a plasticating 3D printer. *J. Rheol.* **61**, 229–236 (2017).
13. T. K. Kirk, R. L. Farrell, Enzymatic "combustion": The microbial degradation of lignin. *Annu. Rev. Microbiol.* **41**, 465–501 (1987).
14. A. J. Ragauskas, G. T. Beckham, M. J. Biddy, R. Chandra, F. Chen, M. F. Davis, B. H. Davison, R. A. Dixon, P. Gilna, M. Keller, P. Langan, A. K. Naskar, J. N. Saddler, T. J. Tschaplinski, G. A. Tuskan, C. E. Wyman, Lignin valorization: Improving lignin processing in the biorefinery. *Science* **344**, 1246843 (2014).
15. C. Wang, S. S. Kelley, R. A. Venditti, Lignin-based thermoplastic materials. *ChemSusChem* **9**, 770–783 (2016).
16. T. Saito, R. H. Brown, M. A. Hunt, D. L. Pickel, J. M. Pickel, J. M. Messman, F. S. Baker, M. Keller, A. K. Naskar, Turning renewable resources into value-added polymer: Development of lignin-based thermoplastic. *Green Chem.* **14**, 3295–3303 (2012).
17. T. Bova, C. D. Tran, M. Y. Balakshin, J. Chen, E. A. Capanema, A. K. Naskar, An approach towards tailoring interfacial structures and properties of multiphase renewable thermoplastics from lignin–nitrile rubber. *Green Chem.* **18**, 5423–5437 (2016).
18. Q. Sun, R. Khunsupat, K. Akato, J. Tao, N. Labbé, N. C. Gallego, J. J. Bozell, T. G. Rials, G. A. Tuskan, T. J. Tschaplinski, A. K. Naskar, Y. Pu, A. J. Ragauskas, A study of poplar organosolv lignin after melt rheology treatment as carbon fiber precursors. *Green Chem.* **18**, 5015–5024 (2016).
19. C. D. Tran, J. Chen, J. K. Keum, A. K. Naskar, A new class of renewable thermoplastics with extraordinary performance from nanostructured lignin-elastomers. *Adv. Funct. Mater.* **26**, 2677–2685 (2016).
20. N. A. Nguyen, K. M. Meek, C. C. Bowland, S. H. Barnes, A. K. Naskar, An acrylonitrile–butadiene–lignin renewable skin with programmable and switchable electrical conductivity for stress/strain-sensing applications. *Macromolecules* **51**, 115–127 (2018).
21. K. Akato, C. D. Tran, J. Chen, A. K. Naskar, Poly(ethylene oxide)-assisted macromolecular self-assembly of lignin in ABS matrix for sustainable composite applications. *ACS Sustain. Chem. Eng.* **3**, 3070–3076 (2015).
22. M. S. Huda, L. T. Drzal, A. K. Mohanty, M. Misra, Effect of fiber surface-treatments on the properties of laminated biocomposites from poly (lactic acid)(PLA) and kenaf fibers. *Comp. Sci. Technol.* **68**, 424–432 (2008).
23. N. A. Nguyen, C. C. Bowland, A. K. Naskar, A general method to improve 3D-printability and inter-layer adhesion in lignin-based composites. *Appl. Mater. Today* **12**, 138–152 (2018).
24. C. Crestini, H. Lange, M. Sette, D. S. Argyropoulos, On the structure of softwood kraft lignin. *Green Chem.* **19**, 4104–4121 (2017).
25. A. L. Holmberg, N. A. Nguyen, M. G. Karavolias, K. H. Reno, R. P. Wool, T. H. Epps III, Softwood lignin-based methacrylate polymers with tunable thermal and viscoelastic properties. *Macromolecules* **49**, 1286–1295 (2016).
26. A. L. Holmberg, K. H. Reno, N. A. Nguyen, R. P. Wool, T. H. Epps III, Syringyl methacrylate, a hardwood lignin-based monomer for high-T_g polymeric materials. *ACS Macro Lett.* **5**, 574–578 (2016).
27. W. P. Cox, E. H. Merz, Correlation of dynamic and steady flow viscosities. *J. Polym. Sci.* **28**, 619–622 (1958).
28. M. L. Williams, R. F. Landel, J. D. Ferry, The temperature dependence of relaxation mechanisms in amorphous polymers and other glass-forming liquids. *J. Am. Chem. Soc.* **77**, 3701–3707 (1955).
29. A. Tuteja, M. E. Mackay, C. J. Hawker, B. Van Horn, Effect of ideal, organic nanoparticles on the flow properties of linear polymers: Non-einstein-like behavior. *Macromolecules* **38**, 8000–8011 (2005).
30. C. Rauwendaal, *Polymer Extrusion* (Carl Hanser Verlag GmbH Co KG, 2014).
31. J. O. Hardin, T. J. Ober, A. D. Valentine, J. A. Lewis, Microfluidic printheads for multimaterial 3D printing of viscoelastic inks. *Adv. Mater.* **27**, 3279–3284 (2015).
32. N. Ladkau, M. Assmann, M. Schrewe, M. K. Julsing, A. Schmid, B. Bühler, Efficient production of the nylon 12 monomer ω-aminododecanoic acid methyl ester from renewable dodecanoic acid methyl ester with engineered *Escherichia coli*. *Metab. Eng.* **36**, 1–9 (2016).
33. S. Kind, S. Neubauer, J. Becker, M. Yamamoto, M. Völkert, G. von Abendroth, O. Zelder, C. Wittmann, From zero to hero—Production of bio-based nylon from renewable resources using engineered *Corynebacterium glutamicum*. *Metab. Eng.* **25**, 113–123 (2014).
34. H. Mutlu, M. A. R. Meier, Unsaturated PA X, 20 from renewable resources via metathesis and catalytic amidation. *Macromol. Chem. Phys.* **210**, 1019–1025 (2009).
35. M. A. R. Meier, J. O. Metzger, U. S. Schubert, Plant oil renewable resources as green alternatives in polymer science. *Chem. Soc. Rev.* **36**, 1788–1802 (2007).
36. G. Cheng, X. Zhang, B. Simmons, S. Singh, Theory, practice and prospects of X-ray and neutron scattering for lignocellulosic biomass characterization: Towards understanding biomass pretreatment. *Energy Environ. Sci.* **8**, 436–455 (2015).
37. B. Y. Ahn, E. B. Duoss, M. J. Motala, X. Guo, S.-I. Park, Y. Xiong, J. Yoon, R. G. Nuzzo, J. A. Rogers, J. A. Lewis, Omnidirectional printing of flexible, stretchable, and spanning silver microelectrodes. *Science* **323**, 1590–1593 (2009).
38. R. B. Rao, K. L. Krafcik, A. M. Morales, J. A. Lewis, Microfabricated deposition nozzles for direct-write assembly of three-dimensional periodic structures. *Adv. Mater.* **17**, 289–293 (2005).
39. J. A. Lewis, J. E. Smay, J. Stuecker, J. Cesarano III, Direct ink writing of three-dimensional ceramic structures. *J. Am. Ceram. Soc.* **89**, 3599–3609 (2006).
40. M. Lis, M. Plaut, A. Zai, D. Cipolle, J. Russo, J. Lewis, T. Fedynyshyn, Polymer dielectrics for 3D-printed rf devices in the K_a band. *Adv. Mater. Technol.* **1**, 1600027 (2016).
41. D. B. Kolesky, R. L. Truby, A. S. Gladman, T. A. Busbee, K. A. Homan, J. A. Lewis, 3D bioprinting of vascularized, heterogeneous cell-laden tissue constructs. *Adv. Mater.* **26**, 3124–3130 (2014).
42. J. T. Muth, D. M. Vogt, R. L. Truby, Y. Mengüç, D. B. Kolesky, R. J. Wood, J. A. Lewis, Embedded 3D printing of strain sensors within highly stretchable elastomers. *Adv. Mater.* **26**, 6307–6312 (2014).
43. B. G. Compton, J. A. Lewis, 3D-printing of lightweight cellular composites. *Adv. Mater.* **26**, 5930–5935 (2014).
44. K. Inoue, S. Hoshino, Crystal structure of nylon 12. *J. Polym. Sci. Part B Polym. Phys.* **11**, 1077–1089 (1973).
45. C. Ramesh, Crystalline transitions in nylon 12. *Macromolecules* **32**, 5704–5706 (1999).
46. M. H. J. Koch, W. H. de Jeu, Crystalline structure and morphology in nylon-12: A small-and wide-angle X-ray scattering study. *Macromolecules* **36**, 1626–1632 (2003).
47. M. Dosière, Orientation of the lamellar crystals in polyamide 12. *Polymer* **34**, 3160–3167 (1993).
48. J. W. Kiel, A. P. R. Eberle, M. E. Mackay, Nanoparticle agglomeration in polymer-based solar cells. *Phys. Rev. Lett.* **105**, 168701 (2010).
49. J. J. Wie, N. A. Nguyen, C. D. Cwalina, J. Liu, D. C. Martin, M. E. Mackay, Shear-induced solution crystallization of poly(3-hexylthiophene) (P3HT). *Macromolecules* **47**, 3343–3349 (2014).
50. J. R. Raney, B. G. Compton, J. Mueller, T. J. Ober, K. Shea, J. A. Lewis, Rotational 3D printing of damage-tolerant composites with programmable mechanics. *Proc. Natl. Acad. Sci. U.S.A.* **115**, 1198–1203 (2018).

Acknowledgments: We thank A. X. Staub and J. L. Long for assistance with the material blending. This manuscript has been authored by UT-Battelle, LLC, under contract DE-AC05-00OR22725 with the U.S. Department of Energy (DOE). The U.S. Government retains, and the publisher, by accepting the article for publication, acknowledges that the U.S. Government retains a nonexclusive, paid-up, irrevocable, worldwide license to publish or reproduce the published form of this manuscript, or allow others to do so, for U.S. Government purposes. DOE will provide public access to these results of federally sponsored research in accordance with the DOE Public Access Plan (http://energy.gov/downloads/doe-public-access-plan). The views and opinions of the authors expressed herein do not necessarily state or reflect those of the U.S. Government or any agency thereof. Neither the U.S. Government nor any agency thereof, nor any of their employees, makes any warranty, expressed or implied, or assumes any legal liability or responsibility for the accuracy, completeness, or usefulness of any information, apparatus, product, or process disclosed, or represents that its use would not

infringe privately owned rights. **Funding:** The research at the Oak Ridge National Laboratory, managed by UT Battelle, LLC, for the U.S. Department of Energy (DOE) under contract DE-AC05-00OR22725, was sponsored by the Office of Energy Efficiency and Renewable Energy BioEnergy Technologies Office Program. J.K.K. and K.C.L. acknowledge the financial support of the Neutron Scattering Division (NSD) of the Oak Ridge National Laboratory (ORNL), which was sponsored by the ORNL Scientific User Facilities Division, DOE Office of Basic Research Sciences. J.K.K. also acknowledges the financial support of the Center for Nanophase Materials Sciences (CNMS) of the Oak Ridge National Laboratory (ORNL), which was sponsored by the ORNL Scientific User Facilities Division, DOE Office of Basic Research Sciences. **Author contributions:** N.A.N. and A.K.N. conceived the scope of the work. N.A.N. designed and performed the research. S.H.B. contributed to the material blending and mechanical testing. C.C.B. contributed to the SEM characterization. K.M.M. contributed to the NMR and GPC characterization of lignins. J.K.K. and K.C.L. contributed to the SANS characterization. N.A.N. and A.K.N. wrote the manuscript with input from all coauthors. A.K.N. directed the research. **Competing interests:** N.A.N. and A.K.N. are the inventors on a patent application (Invention Disclosure 201703895, DOE S-138,553) and a provisional patent application filed by UT Battelle, LL (No. 62/621,705, filed 25 January 2018). All other authors declare that they have no competing interests. **Data and materials availability:** All data needed to evaluate the conclusions in the paper are present in the paper and/or the Supplementary Materials. Additional data related to this paper may be requested from the authors.

Submitted 5 March 2018
Accepted 15 November 2018
Published 14 December 2018
10.1126/sciadv.aat4967

Citation: N. A. Nguyen, S. H. Barnes, C. C. Bowland, K. M. Meek, K. C. Littrell, J. K. Keum, A. K. Naskar, A path for lignin valorization via additive manufacturing of high-performance sustainable composites with enhanced 3D printability. *Sci. Adv.* **4**, eaat4967 (2018).

A path for lignin valorization via additive manufacturing of high-performance sustainable composites with enhanced 3D printability

Ngoc A. Nguyen, Sietske H. Barnes, Christopher C. Bowland, Kelly M. Meek, Kenneth C. Littrell, Jong K. Keum and Amit K. Naskar

Sci Adv **4** (12), eaat4967.
DOI: 10.1126/sciadv.aat4967